







Isolated copper single sites for high-performance electroreduction of carbon monoxide to multicarbon products

Haihong Bao^{1,11}, Yuan Qiu^{1,11}, Xianyun Peng^{1,11}, Jia-ao Wang^{2,11}, Yuying Mi¹, Shunzheng Zhao³, Xijun Liu^{1,4}, Yifan Liu⁵, Rui Cao⁶, Longchao Zhuo⁷, Junqiang Ren⁸, Jiaqiang Sun⁹, Jun Luo¹ & Xuping Sun¹⁰

Electrochemical carbon monoxide reduction is a promising strategy for the production of value-added multicarbon compounds, albeit yielding diverse products with low selectivities and Faradaic efficiencies. Here, copper single atoms anchored to $\text{Ti}_3\text{C}_2\text{T}_x$ MXene nanosheets are firstly demonstrated as effective and robust catalysts for electrochemical carbon monoxide reduction, achieving an ultrahigh selectivity of 98% for the formation of multicarbon products. Particularly, it exhibits a high Faradaic efficiency of 71% towards ethylene at -0.7 V versus the reversible hydrogen electrode, superior to the previously reported copper-based catalysts. Besides, it shows a stable activity during the 68-h electrolysis. Theoretical simulations reveal that atomically dispersed Cu-O₃ sites favor the C-C coupling of carbon monoxide molecules to generate the key *CO-CHO species, and then induce the decreased free energy barrier of the potential-determining step, thus accounting for the high activity and selectivity of copper single atoms for carbon monoxide reduction.

¹Institute for New Energy Materials & Low-Carbon Technologies and Tianjin Key Lab of Photoelectric Materials & Devices, School of Materials Science and Engineering, Tianjin University of Technology, Tianjin 300384, China. ²School of Material Science and Engineering, University of Jinan, Jinan 250022, China. ³Department of Environmental Engineering, University of Science and Technology Beijing, Beijing 100083, China. ⁴Key Laboratory of Civil Aviation Thermal Hazards Prevention and Emergency Response, Civil Aviation University of China, Tianjin 300300, China. ⁵College of Physics and Optoelectronic Engineering, Shenzhen University, Shenzhen 518060, China. ⁶Stanford Synchrotron Radiation Lightsource, SLAC National Accelerator Laboratory, Menlo Park, CA 94025, United States. ⁷School of Materials Science and Engineering, Xi'an University of Technology, Xi'an 710048 Shanxi, China. ⁸State Key Laboratory of Advanced Processing and Recycling of Nonferrous Metals, Lanzhou University of Technology, Lanzhou 730050 Gansu, China. ⁹State Key Laboratory of Coal Conversion, Institute of Coal Chemistry, Chinese Academy of Sciences, Taiyuan 030001 Shanxi, China. ¹⁰Institute of Fundamental and Frontier Sciences, University of Electronic Science and Technology of China, Chengdu 610054 Sichuan, China. ¹¹These authors contributed equally: Haihong Bao, Yuan Qiu, Xianyun Peng, Jia-ao Wang. ✉email: xjliu@tjut.edu.cn; caorui@stanford.edu; xpsun@uestc.edu.cn

The electrochemical CO₂ reduction (CO₂R), as an appealing approach toward CO₂ mitigation and artificial carbon recycling, has been extensively studied in recent years^{1–4}. However, effective strategies for the direct reduction of CO₂ to more value-added C₂₊ products are not available at present due to the relatively low selectivity. In contrast, a wealth of efficient and selective electrocatalysts have been developed for the reduction of CO₂ to CO as the primary product, achieving a Faradaic efficiency (FE) larger than 90%^{5–7}. In this regard, the further electrochemical CO reduction (COR) is desirable for deriving more value-added C₂₊ products^{6,8–10}.

Abundant efforts have been made in developing efficient COR catalysts^{11–13}, however, to date, copper (Cu)-based materials are still the only known metal catalysts for electrochemically converting CO into multicarbon hydrocarbons and oxygenates, like C₂H₄ and C₂H₅OH (EtOH), with an appreciable activity^{14–17}. Generally, the stepped or kinked surfaces, as well as grain boundary surface terminations in polycrystalline Cu and oxide-derived Cu species^{11,18,19}, are considered to be active for COR. However, the structural complexity of these Cu species imposes a lot of difficulties to identify the exact sites responsible for their catalytic properties. Moreover, the diverse active centers of Cu species lead to unsatisfactory FEs and selectivities of the desired products because of various undetermined reaction pathways and competing hydrogen evolution reaction (HER). In contrast, single-atom (SA) catalysts exhibit unique active centers that can acquire an exceptional activity and selectivity in those electrocatalysis reactions involving multiple pathways^{20–23}. Therefore, SA-based materials present potentially promising alternative catalysts, although they have never been scrutinized as COR electrocatalysts until now.

Recently, the two-dimensional (2D) materials, as a powerful platform to support SA catalysts, have attracted great attention because of large specific surface areas, more exposed active sites, and superior catalytic activities^{24–30}. Particularly, with excellent electronic conductivity, catalytically active basal planes, and graphene-like unique layered structures, 2D Ti₃C₂T_x MXene (T_x represents surface functional groups) has been investigated extensively for a variety of electrochemical reactions^{31–33}. More importantly, it has a unique feature of a high reducing capability, suitable surface defects, and hydrophilic surface functionalities, which make it an ideal candidate to support and stabilize SAs^{34,35}.

In this work, we disclose the synthesis, characterization, and COR activity of the Cu SA catalyst stabilized on 2D Ti₃C₂T_x nanosheets. The supported Cu SA catalysts corresponded to O-coordinated Cu sites on Ti₃C₂T_x matrix (Cu-SA/Ti₃C₂T_x), as revealed by X-ray absorption fine structure (XAFS) analysis. Computational studies confirmed the outstanding stability of Cu SAs on Ti₃C₂T_x. When applied in COR, Cu-SA/Ti₃C₂T_x shows unprecedented selectivity (98% total) in the formation of C₂ products, which is much higher than its counterpart of Cu-NP/Ti₃C₂T_x. Outstandingly, the maximum FE of 71% towards C₂H₄ is achieved at –0.7 V versus the reversible hydrogen electrode (vs RHE), representing one of the highest values among the reported Cu-based COR catalysts^{1,5,8–13}. Furthermore, Cu-SA/Ti₃C₂T_x presents high electrochemical stability over 68 h. Theoretical analysis of pathways for C₂H₄ and EtOH formation gives an in-depth understanding of the enhanced reactivity and selectivity of Cu-SA/Ti₃C₂T_x compared with Cu nanoparticles.

Results

Synthesis and characterization of Cu-SA/Ti₃C₂T_x. As illustrated in Fig. 1a, ultrathin Ti₃C₂T_x nanosheets were prepared from parent Ti₃AlC₂ via etching in a mixed solution of HCl and LiF, and Cu-SA/Ti₃C₂T_x was achieved by a one-step synthesis strategy

(see the Methods section for more details). The X-ray diffraction (XRD) pattern of Cu-SA/Ti₃C₂T_x, as shown in Fig. 1b, reveals a crystal structure similar to that of Ti₃C₂T_x (ref. 33). No diffraction peaks of any Cu species are observed, indicating the good dispersion of Cu SAs on Ti₃C₂T_x. High-angle annular dark-field scanning transmission electron microscopy (HAADF-STEM) and transmission electron microscopy (TEM) images clearly indicate a nanosheet morphology of the as-synthesized Cu-SA/Ti₃C₂T_x (Supplementary Figs. 1, 2 and Fig. 1c). Cu-SA/Ti₃C₂T_x exhibits some interlayer-stacked mesopores resulting from the nanosheet structure (Supplementary Fig. 3), which improves the accessibility of active sites, and thus, the overall catalytic performance of the catalyst³⁶. No Cu particles are visible in the TEM images (Fig. 1c and Supplementary Fig. 2), which correlates well with the XRD results (Fig. 1b). Atomic-resolution HAADF-STEM images (Fig. 1d and Supplementary Fig. 4) taken from randomly selected regions show individual Cu atoms (sharp bright dots) uniformly dispersed on the Ti₃C₂T_x crystal lattice fringes. The presence of Cu SAs can also be confirmed by the simulated HAADF-STEM images in Supplementary Fig. 5 and comparisons with the images of Ti₃C₂T_x support in Supplementary Fig. 6. Besides, statistical analysis indicated that the average distance between each Cu atom is determined to be 0.61 nm (Supplementary Fig. 7), much higher than that of Cu–Cu bond (~0.27 nm) in Cu dimers. Even a small number of Cu pairs (<4%) are potentially formed, but such a small portion does very little contribution to the high COR activity. Energy-dispersive X-ray spectroscopy (EDX) further demonstrates the homogenous distribution of Ti, C, O, and Cu atoms over the Cu-SA/Ti₃C₂T_x surface (Supplementary Fig. 8). A Cu loading of 0.2 wt% was determined by inductively coupled plasma optical emission spectrometry (ICP-OES). In addition, when more Cu precursor was added, the co-existence of Cu SAs and abundant Cu nanoclusters could be observed in the Ti₃C₂T_x support (denoted as Cu-NC/Ti₃C₂T_x, Supplementary Fig. 9).

The chemical structure of Cu anchored to Ti₃C₂T_x was further confirmed by X-ray photoelectron spectrometry (XPS) and X-ray absorption spectroscopy (XAS). The Cu 2*p* XPS spectrum of Cu-SA/Ti₃C₂T_x (Supplementary Fig. 10) reveals binding energies of 932.5 and 952.4 eV for Cu 2*p*_{3/2} and 2*p*_{1/2} orbitals, respectively, which are close to those of Cu⁰ or Cu¹⁺ (refs. 37,38). X-ray absorption near-edge structure (XANES) and extended X-ray absorption fine structure (EXAFS), which have been widely used for characterizing the SA catalysts in pioneering works^{39,40}, were performed at the Cu K-edge. The Cu foil, Cu₂O, and CuO were also tested as a comparison to Cu-SA/Ti₃C₂T_x. The XANES profiles (Fig. 1e) suggest that the Cu valence state in Cu-SA/Ti₃C₂T_x is likely to be higher than that of metallic Cu⁰ but lower than that of Cu¹⁺. The Fourier transform-EXAFS (FT-EXAFS) curve of Cu-SA/Ti₃C₂T_x (Fig. 1f) shows one main peak at about 1.6 Å, and no prominent Cu–Cu back-scattering peak (2.2 Å, existed in Cu foil EXAFS spectra) is observed^{23,41}. The wavelet transform (WT) contour plot of the Cu K-edge EXAFS oscillations of Cu-SA/Ti₃C₂T_x (Supplementary Fig. 11) shows one intensity maximum at 4.0 Å^{–1} associated with the Cu–O path in the first coordination shell. Compared with the WT plot of the Cu foil, no intensity maximum is detected near 7.7 Å^{–1} (corresponding to the Cu–Cu path), this provides further evidence for the atomic dispersion of Cu atoms. According to the fitting results shown in Fig. 1g and Supplementary Fig. 12, the main peak at ~1.6 Å is associated with the nearest O coordination shell of the Cu-SA/Ti₃C₂T_x catalyst (phase uncorrected). The small bulge at a radical distance of ~2.7 Å is associated with the scattering path of the second shell Ti, which is in agreement with the theoretical optimized model (inset of Fig. 1g). The fitted parameters are listed in Supplementary Table 1 and the coordination number of O is ~3. Therefore, Cu–O₃ sites formed

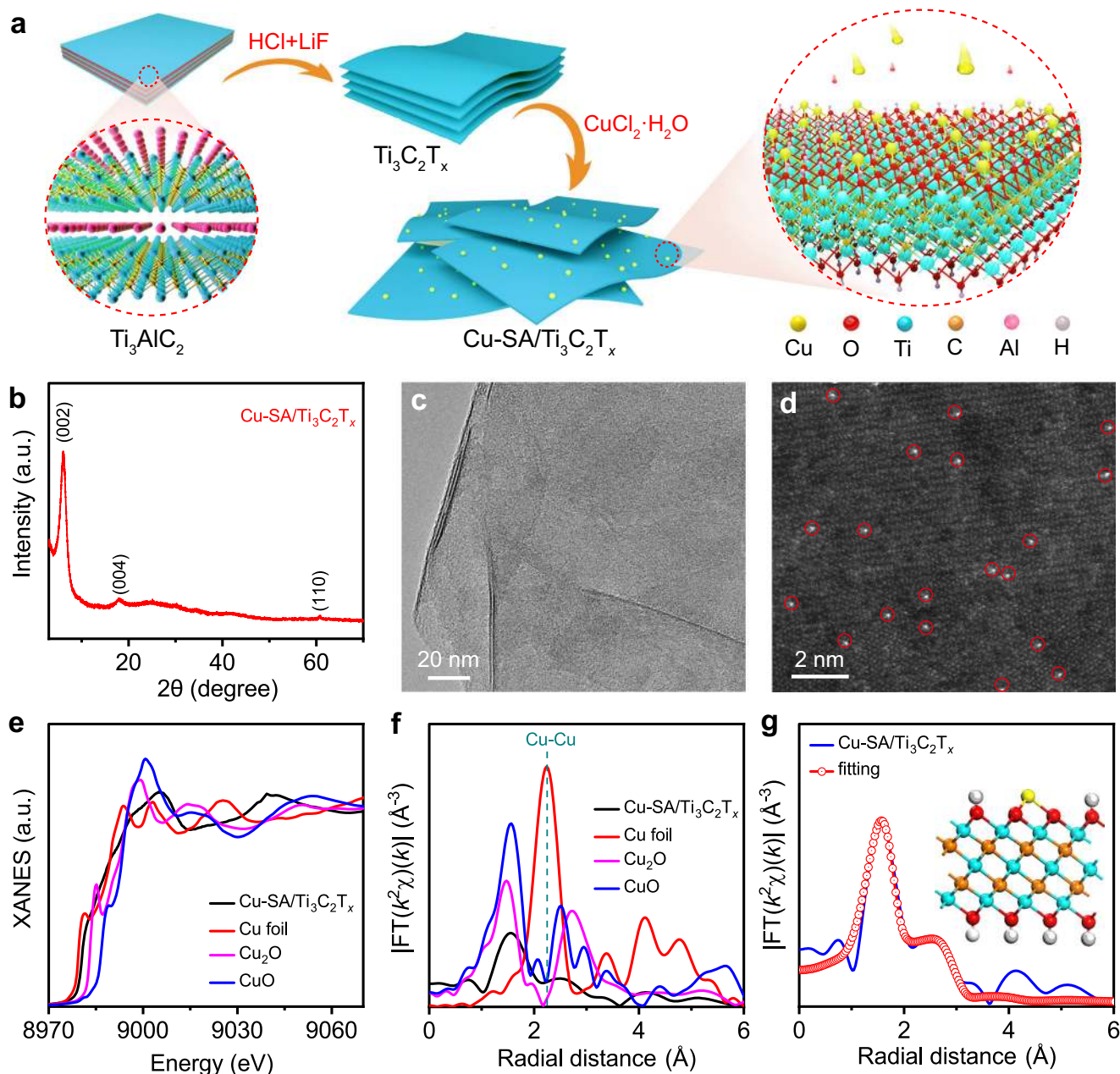


Fig. 1 Preparation and structural characterization of Cu-SA/Ti₃C₂T_x. **a** Schematic illustration of the synthesis procedure. **b** XRD pattern. **c** TEM image. **d** HAADF-STEM image in which some of the Cu SAs are highlighted by red circles. **e** XANES spectra at the Cu K-edge with CuO, Cu₂O and Cu foil as reference. **f** The k^2 -weighted Fourier transform (FT) EXAFS curves in which $\chi(k)$ denotes the EXAFS oscillation function. **g** EXAFS fitting curve of Cu-SA/Ti₃C₂T_x, insert is an illustration of Cu-SA/Ti₃C₂T_x structure. The yellow, blue, dark yellow, red and white balls represent Cu, Ti, C, O and H, respectively.

in Cu-SA/Ti₃C₂T_x (inset of Fig. 1g). Moreover, the Bader charge analysis of the optimized model indicates that Cu SAs in Cu-SA/Ti₃C₂T_x are positively charged (+0.42, Supplementary Fig. 13), in line with XANES result (Fig. 1e). Unfortunately, the CO diffuse reflectance infrared Fourier transform spectroscopy (CO-DRIFTS) measurement under ambient conditions failed to probe the dispersion of Cu in Cu-SA/Ti₃C₂T_x (Supplementary Fig. 14), probably because of the weakening CO adsorption on the surface of Cu-SA/Ti₃C₂T_x without an applied bias voltage. Since the oxygen atoms are part of T_x surface groups, this suggests that the Cu atoms are dispersed on the surface of the Ti₃C₂T_x nanosheets.

COR performance of Cu-SA/Ti₃C₂T_x in the alkaline system.

COR properties of Cu-SA/Ti₃C₂T_x were evaluated using a

Nafion-separated H-type cell with CO-saturated 1 M KOH as electrolyte. The potentials were converted to the RHE scale. Linear sweep voltammetry (LSV; Fig. 2a) shows that the current densities (normalized by the geometrical surface area) increase with increasing applied potential. The current density of Cu-SA/Ti₃C₂T_x in CO-purged electrolyte is distinctly higher than that under Ar atmosphere, demonstrating good electrocatalytic activity toward the COR. Electrolysis was performed in a potential range of -0.4 to -0.9 V vs RHE for 2 h at each constant potential. The gas and liquid products were quantified by gas chromatography (GC) and ¹H nuclear magnetic resonance (NMR) spectroscopy, respectively, in which dimethyl sulfoxide (DMSO) was used as an internal standard (Supplementary Fig. 15).

Figure 2b shows the FEs of the reduction products as well as the competing hydrogen formation on Cu-SA/Ti₃C₂T_x at the

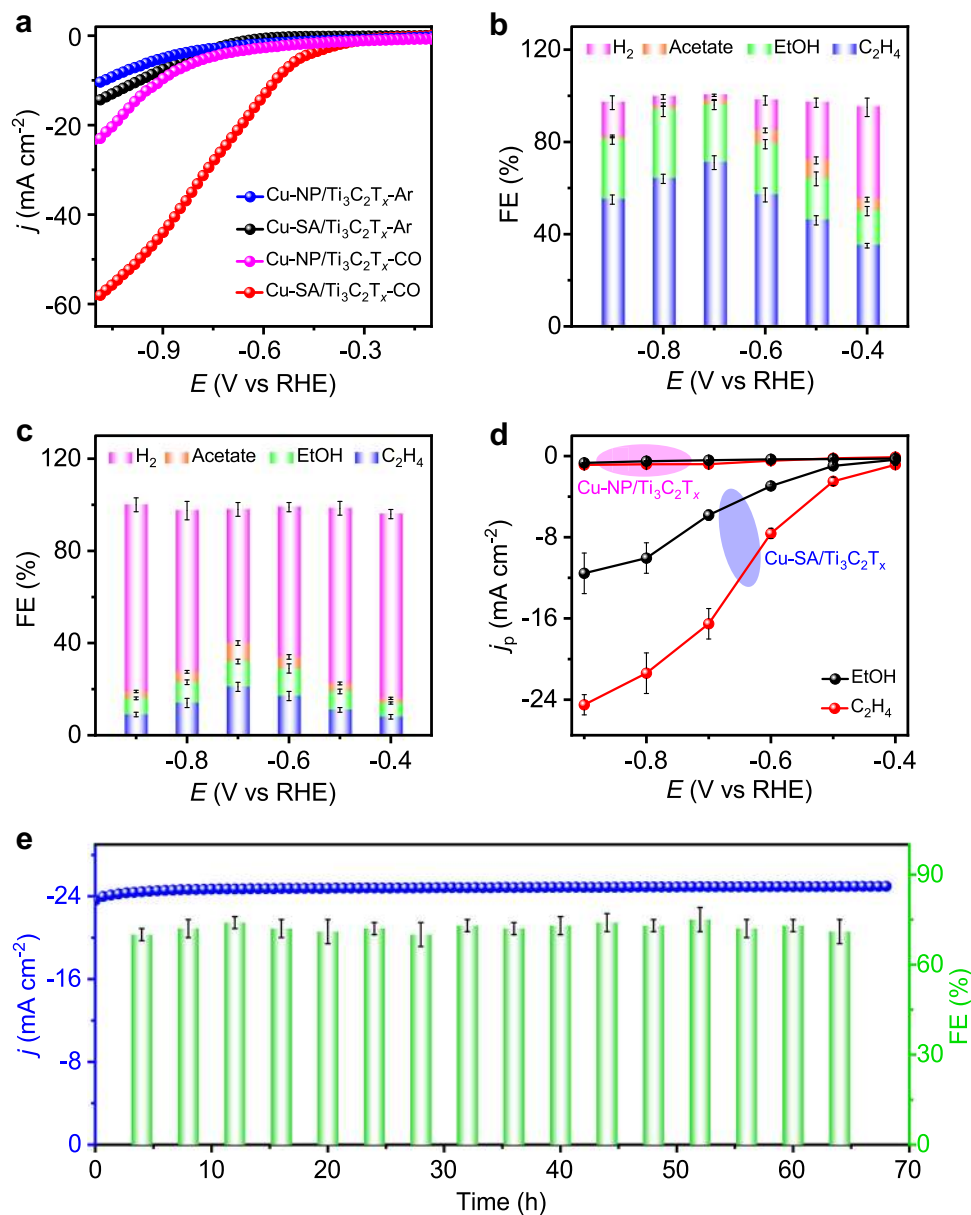


Fig. 2 Electrochemical CO reduction performances. **a** Linear sweep voltammograms of Cu-SA/Ti₃C₂T_x measured in CO- or Ar-saturated 1 M KOH solution at a scan rate of 10 mV s⁻¹; potentials have been *iR*-corrected. **b, c** Faradaic efficiencies (FE) toward H₂ and CO reduction products (C₂H₄, EtOH, and acetate) of **b** Cu-SA/Ti₃C₂T_x and **c** Cu-NP/Ti₃C₂T_x at various applied potentials for 2 h. **d** The partial current densities (*j_p*) of C₂H₄ and EtOH at test potentials. **e** Chronoamperometry test and FE of C₂H₄ for Cu-SA/Ti₃C₂T_x at an applied constant potential of -0.7 V vs RHE for 68 h. The error bars correspond to the standard deviations of measurements over three separately prepared samples under the same testing conditions.

applied potentials. A high total FE of 98% (-0.7 V vs RHE) for C₂ products has been achieved, suggesting the effective suppression of the competing HER. This value is comparable with those of Cu nanoflowers⁴² (~100% FE for C₂₊ products) and Cu nanoparticles⁹ (~91% FE for C₂₊ products). In the wide potential range from -0.6 to -0.9 V vs RHE, C₂ production reveals a total product selectivity of more than 79%, which declined at more negative potentials due to mass transport limitations of CO^{5,43}. C₂H₄ is exclusively produced as the gas product of COR for Cu-SA/Ti₃C₂T_x, obtaining a maximum FE of 71% at -0.7 V vs RHE, which is significantly larger than the highest value of 52.7% reported for Cu NPs⁴⁴ (Supplementary Table 2). Meantime, in the liquid product, the FE of EtOH for Cu-SA/Ti₃C₂T_x reached the highest value of 30% at -0.8 V vs RHE. At -0.7 V vs RHE, the FEs of EtOH and acetate for Cu-SA/Ti₃C₂T_x were 25.0 and 2.2%,

respectively, and the corresponding formation rates are 2.79 and 0.44 mM h⁻¹, respectively (Supplementary Fig. 16). Furthermore, the partial current densities (*j_p*) of C₂H₄ and EtOH for Cu-SA/Ti₃C₂T_x were as high as -16.5 and -5.8 mA cm⁻², respectively, at -0.7 V vs RHE (Fig. 2d).

Cu-SA/Ti₃C₂T_x shows good stability over 68 h electrolysis after the initial activation of the catalyst layer in the first 30 min (Fig. 2e). An average current density of -24.8 mA cm⁻² is observed over the time of the long-term electrolysis. The corresponding FE for C₂H₄ is larger than 70% along with a ~3% oscillation caused by bubble accumulation and a sudden flush out¹². HAADF-STEM images, as well as XRD and XPS results of Cu-SA/Ti₃C₂T_x after electrochemical testing, indicate the well-preserved single Cu sites without the presence of any clusters and particles (Supplementary Figs. 17–19). Additional

density-functional-theory (DFT) calculations further confirmed the high kinetic stability of Cu SAs during the electrolysis (Supplementary Figs. 20 and 21).

To confirm the origins of carbon in the COR products, isotopic labeling experiments were performed by using ^{13}C as the feeding gas. The ^{13}C -labeled reduction products were analyzed by a quadrupole-type mass spectrometer (MS). Dominant peaks of $^{13}\text{C}\text{-C}_2\text{H}_4$ ($m/z = 30$), $^{13}\text{C}\text{-EtOH}$ ($m/z = 47$), and $^{13}\text{C}\text{-acetic acid}$ ($m/z = 62$) were observed (Supplementary Figs. 22–24)^{45–47}. The evidence confirms that the evolved reduction products derive from the CO electrolysis over Cu-SA/ $\text{Ti}_3\text{C}_2\text{T}_x$. In addition, the generated EtOH can also be excluded from the residual EtOH in preparing the working electrode (Supplementary Fig. 25).

As a comparison, Cu particles (10–50 nm) supported on $\text{Ti}_3\text{C}_2\text{T}_x$ (denoted as Cu-NP/ $\text{Ti}_3\text{C}_2\text{T}_x$; Supplementary Figs. 26–30) were also prepared with a Cu loading of 5.2 wt%. Cu-NP/ $\text{Ti}_3\text{C}_2\text{T}_x$ shows a very low current density of -16.2 mA cm^{-2} at -1.0 V vs RHE (Fig. 2a), which is 3.2-fold lower than that on Cu-SA/ $\text{Ti}_3\text{C}_2\text{T}_x$ (-52.2 mA cm^{-2}). The highest FEs of C_2H_4 and EtOH were only 21% (-0.7 V vs RHE) and 12% (-0.6 V vs RHE), respectively, in the electrocatalytic process on Cu-NP/ $\text{Ti}_3\text{C}_2\text{T}_x$ (Fig. 2c), which are about 3.4- and 2.1-fold lower than on Cu-SA/ $\text{Ti}_3\text{C}_2\text{T}_x$, respectively. In addition, the calculated formation rates of EtOH and acetate for Cu-NP/ $\text{Ti}_3\text{C}_2\text{T}_x$ were 0.19 and 0.31 mM h^{-1} at -0.7 V vs RHE, respectively (Supplementary Fig. 16). H_2 production dominated the whole potential range, showing an FE of 59–81% (Fig. 2c). The influence of Cu NP loading amount in Cu-NP/ $\text{Ti}_3\text{C}_2\text{T}_x$ for the COR performance was also investigated. With an increase of Cu precursor in the synthetic process (Supplementary Figs. 30 and 31), ICP-OES results revealed that the Cu content in Cu-NP/ $\text{Ti}_3\text{C}_2\text{T}_x$ increased from 5.2 to 9.8 and 20.3 wt%, respectively. We found that the two additional Cu-NP/ $\text{Ti}_3\text{C}_2\text{T}_x$ control samples showed relatively improved COR activities (Supplementary Fig. 32); however, their performances are still inferior to those of Cu-SA/ $\text{Ti}_3\text{C}_2\text{T}_x$ (Fig. 2a, b), suggesting that the Cu NP content is not the major contribution to the COR activity.

Meanwhile, the other two samples of pristine $\text{Ti}_3\text{C}_2\text{T}_x$ (Supplementary Fig. 6) and reduced $\text{Ti}_3\text{C}_2\text{T}_x$ (namely R- $\text{Ti}_3\text{C}_2\text{T}_x$, Supplementary Fig. 33) were prepared as comparison. As seen in Supplementary Figs. 34 and 35, the maximum FEs of C_2H_4 formation for $\text{Ti}_3\text{C}_2\text{T}_x$ and R- $\text{Ti}_3\text{C}_2\text{T}_x$ were 7.5% (-0.8 V vs RHE) and 5.2% (-0.7 V vs RHE), respectively, both of them are significantly lower than that of Cu-SA/ $\text{Ti}_3\text{C}_2\text{T}_x$. This finding demonstrates that the $\text{Ti}_3\text{C}_2\text{T}_x$ support helps to capture and stabilize Cu species and the impact on the selectivity of COR is negligible. The high performance of Cu-SA/ $\text{Ti}_3\text{C}_2\text{T}_x$ comes from the atomically dispersed Cu-related active sites.

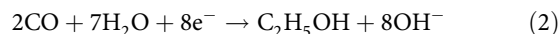
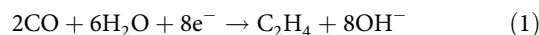
To further confirm the activity of Cu SAs, the COR activity of Cu-SA/ $\text{Ti}_3\text{C}_2\text{T}_x$ was examined in electrolyte containing 0.1 mM KSCN. SCN^- anions are known to coordinate with Cu and poison the single Cu sites^{48,49}. In the presence of SCN^- , Cu-SA/ $\text{Ti}_3\text{C}_2\text{T}_x$ exhibits a noticeable decay in current density (Supplementary Fig. 36). Meanwhile, the obtained highest FE_{C_2} of Cu-SA/ $\text{Ti}_3\text{C}_2\text{T}_x$ is as low as 26% (-0.7 V vs. RHE), much smaller than that of electrolyte without SCN^- (Fig. 2b). These results strongly demonstrate that Cu single atoms act as the COR sites.

The increased electrochemical active surface area (ECSA) and interfacial charge transfer rate (Supplementary Figs. 37 and 38) may be potentially accounted for the enhanced COR activity of Cu-SA/ $\text{Ti}_3\text{C}_2\text{T}_x$. As shown in Supplementary Fig. 39, the ECSA-corrected LSV results depict a much better catalytic current density of Cu-SA/ $\text{Ti}_3\text{C}_2\text{T}_x$ in comparison with Cu-NP/ $\text{Ti}_3\text{C}_2\text{T}_x$, implying that the presence of Cu SAs resulted in higher intrinsic activity. According to a previous study⁴², the inferior COR

performance of Cu-NP/ $\text{Ti}_3\text{C}_2\text{T}_x$ might result from the smaller ECSA in comparison with Cu-SA/ $\text{Ti}_3\text{C}_2\text{T}_x$, which make it favor the competitive hydrogen evolution.

Theoretical insights on COR activity. To elucidate the COR activity, the mechanistic regimes for the formation of C_2H_4 and EtOH on Cu-SA/ $\text{Ti}_3\text{C}_2\text{T}_x$ catalyst was parsed by calculating key intermediates and favorable reaction pathways in each primitive reaction, as shown in Fig. 3a, c and Supplementary Fig. 40. Generally, the $\text{Ti}_3\text{C}_2\text{T}_x$ surface is functionalized with T_x groups, including $-\text{O}$, $-\text{OH}$, and $-\text{F}$. As revealed by the electron energy loss spectroscopy (EELS) spectrum in Supplementary Fig. 41, the residual F content in Cu-SA/ $\text{Ti}_3\text{C}_2\text{T}_x$ is very low in comparison with O. Moreover, the $-\text{F}$ is thermodynamically unfavorable compared with $-\text{O}$ and $-\text{OH}$ moieties⁵⁰. In addition, in an aqueous solution, the $-\text{O}$ termination would become hydroxylated under the electrocatalysis according to the surface Pourbaix diagrams⁵¹. Therefore, in this work, the $-\text{OH}$ terminated Cu-SA/ $\text{Ti}_3\text{C}_2\text{T}_x$ model was employed, and the solvent effect is also considered using the implicit solvation model⁵². The primitive reaction on Cu (111) surface (Supplementary Fig. 27), which represents the predominate exposed active surface of Cu-NP/ $\text{Ti}_3\text{C}_2\text{T}_x$, was also computed as a comparison.

The overall total reaction processes of C_2H_4 and EtOH are indicated below in equations (1) and (2), both of them are formed in $8e^-$ reductions with H_2O as the H^+ source:



Since that the $2^*\text{CO} \rightarrow ^*\text{COCO}$ process failed to proceed on Cu-SA/ $\text{Ti}_3\text{C}_2\text{T}_x$ due to the large Cu-Cu distance in the catalyst (Supplementary Fig. 42), the $^*\text{CHO}$ pathway is considered for Cu-SA/ $\text{Ti}_3\text{C}_2\text{T}_x$ (Fig. 3b). Firstly, one CO molecule adsorbed on the Cu SA site, resulting in the formation of $^*\text{CO}$ species (* denotes a binding site), and then $^*\text{CHO}$ formed by one proton transfer process. Next, $^*\text{CHO}$ was coupled with another CO by $^*\text{CHO} + \text{CO} \rightarrow ^*\text{CHO-CO}$ (refs. 53,54) with a free energy barrier of 0.32 eV, which is the rate-limiting step (RLS) during the whole COR process. For Cu (111), two C-C coupling pathways were calculated. $^*\text{CO}$ can be first hydrogenated into $^*\text{COH}$ with a free energy barrier of 1.18 eV (Supplementary Fig. 43), or two $^*\text{CO}$ coupled directly to form $^*\text{COCO}$ with a free energy barrier of 0.94 eV (Fig. 3b and Supplementary Fig. 44)^{55,56}. The large free energy for these two C-C coupling step implies high-energy barriers for the CO-to- C_2 process, consistent with experimentally observed COR performance (Fig. 2c). To further verify the activation energy of the RLS, the climbing image nudged elastic band (CI-NEB) method was employed to calculate the transition states. As shown in Supplementary Fig. 45, the activation barrier for $^*\text{CHO-CO}$ formation on Cu-SA/ $\text{Ti}_3\text{C}_2\text{T}_x$ is as low as 0.82 eV, which is much lower than that of the C-C coupling step on Cu (111) surface (1.36 eV). Therefore, this lower energy demand in the RLS of Cu-SA/ $\text{Ti}_3\text{C}_2\text{T}_x$ accounts for its outstanding COR performance. In addition, the COR pathway was also calculated on pure $\text{Ti}_3\text{C}_2\text{T}_x$ as shown in Supplementary Fig. 46. It indicated that a large energy barrier of 1.29 eV is required for the activation of CO on $\text{Ti}_3\text{C}_2\text{T}_x$, much higher than that on Cu-SA/ $\text{Ti}_3\text{C}_2\text{T}_x$. This agrees well with the poor COR performance of $\text{Ti}_3\text{C}_2\text{T}_x$ as discussed above.

The production selectivity of the COR reaction of Cu-SA/ $\text{Ti}_3\text{C}_2\text{T}_x$ was then discussed. Overall, the reaction pathways to C_2H_4 and EtOH were identical in their beginning $4e^-$ transfer process^{57,58}, which initially resulted in the formation of the $^*\text{C-CHOH}$. After that, the proton-electron transfer of $^*\text{C-CHOH}$

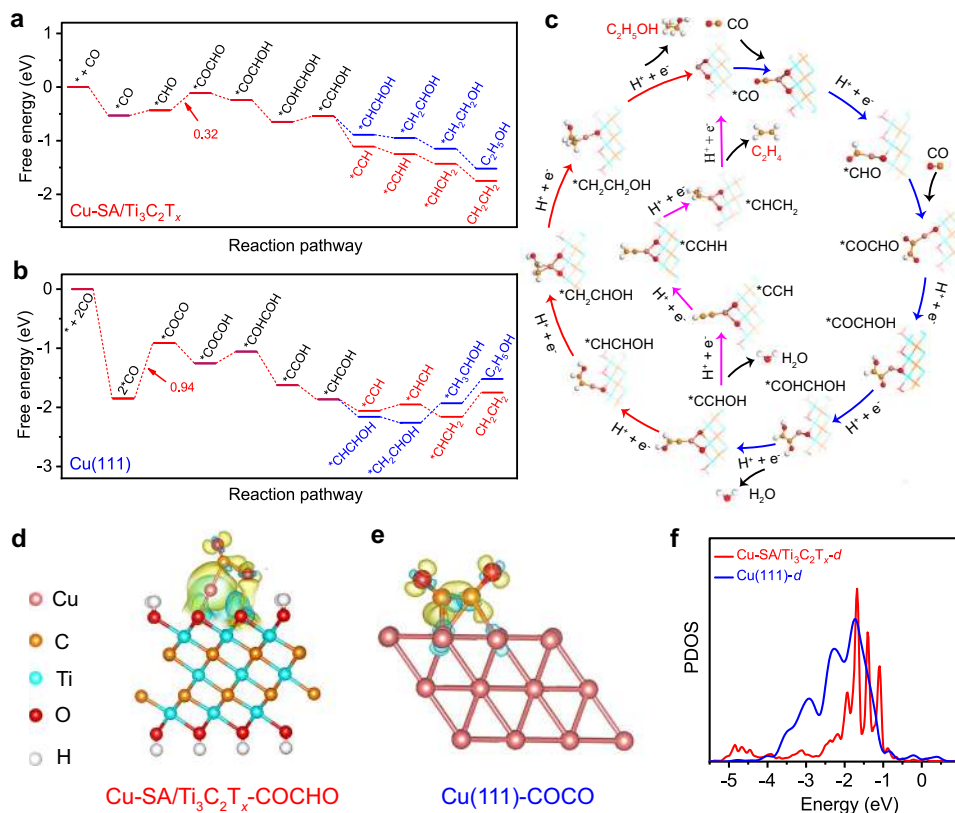


Fig. 3 The optimized energy pathway for CO reduction toward C_2H_4 and EtOH on Cu-SA/ $Ti_3C_2T_x$. **a, b** Free energy diagrams of CO reduction over **a** Cu-SA/ $Ti_3C_2T_x$ and **b** Cu (111). The reason for choosing Cu (111) is that Supplementary Fig. 27 indicates the preferential orientation of the Cu nanoparticles in Cu-NP/ $Ti_3C_2T_x$ is $<111>$. **c** Schematic representation of CO reduction reaction pathways. In some adsorption configurations, Cu-O bond was elongated to get the lowest energy state. **d, e** Charge density difference of the $*COCHO$ -adsorbed and $*COCO$ -adsorbed configuration in **d** Cu-SA/ $Ti_3C_2T_x$ and **e** Cu (111), respectively. **f** The projected densities of states (PDOS) of d -orbitals in Cu-SA/ $Ti_3C_2T_x$ and Cu (111) with an aligned Fermi level. Yellow and blue shadows represent charge accumulation and depletion in the space, respectively; the pinkish-orange, blue, dark yellow, red, and white spheres represent Cu, Ti, C, O, and H, respectively.

splits the pathway to C_2H_4 from the pathway to EtOH. The free energy drop of the $*C-CHOH \rightarrow *C-CH$ (-0.62 eV) toward the formation of C_2H_4 is greater than that of the analog and competitive step $*C-CHOH \rightarrow *CH-CHOH$ (-0.45 eV) in the EtOH formation pathway, suggesting a higher selectivity toward C_2H_4 formation. This may be caused by the greater C-C π bond unsaturation of $*C-CH$ compared with $*CH-CHOH$, which leads to a more stable absorption on the surface of catalysts^{56,59}. Similar results can also be observed in CO_2R process, generally, the production of C_2H_4 was higher than EtOH (refs. 59–61).

Moreover, charge accumulation and depletion between C and Cu atoms are observed on the charge density difference maps of both Cu-SA/ $Ti_3C_2T_x$ and Cu (111) surfaces (Fig. 3d, e), which is an indicator for successful adsorption of key intermediates on the catalyst surfaces. To further elucidate the electronic structures, we compared the projected densities of states (PDOS) of the d -orbitals of Cu-SA/ $Ti_3C_2T_x$ and Cu (111). It is found that the peak of the d -orbital of Cu-SA/ $Ti_3C_2T_x$ is narrower than that of Cu (111) and shifts toward the Fermi level, demonstrating promoted electron transport, and thus, higher reactivity (Fig. 3f)^{62,63}. In addition, the ideal selectivity of Cu-SA/ $Ti_3C_2T_x$ toward C_2H_4 and EtOH formation can also be attributed to the uniform catalytic sites resulting from the certain and simple structure, suppressing the formation of key intermediates toward diverse products (Supplementary Fig. 40). In contrast, the high selectivity nature for conventional catalysts is typically difficult to possess due to their diverse and complicated active sites. These theoretical calculation

results provide some mechanistic explanations for the good activity of Cu-SA/ $Ti_3C_2T_x$.

Additional DFT calculations were performed to determine the free energy (ΔG_{H^*}) of H adsorption on the catalyst surface, which has been identified as a descriptor of HER, as shown in Supplementary Fig. 47. It shows that the ΔG_{H^*} of Cu-SA/ $Ti_3C_2T_x$ is -0.35 eV, much more negative than that on the Cu-NP/ $Ti_3C_2T_x$ ($+0.18$ eV). Accordingly, the proceeding of the HER process on the Cu-SA/ $Ti_3C_2T_x$ surface is more difficult than on the Cu-NP/ $Ti_3C_2T_x$, agrees well with the experimental results in Fig. 2b, c.

In summary, Cu SAs were successfully anchored to $Ti_3C_2T_x$ nanosheets (Cu-SA/ $Ti_3C_2T_x$) and firstly used as catalysts for the COR. Cu-SA/ $Ti_3C_2T_x$ exhibits an ultrahigh selectivity of 98% for the formation of C_2 products and unprecedented selectivity for C_2H_4 production (71%). Experiment and theoretical calculations revealed that the O-coordinated Cu SAs are stable during the electrolysis. For COR, it can promote the formation of the key $*CO-CHO$ intermediate, and collectively decrease the free energy barrier of the rate-determining step. Overall, we speculate that the good selectivity of Cu-SA/ $Ti_3C_2T_x$ toward the formation of C_2H_4 and EtOH can be attributed to its good reactivity and structural simplicity. Our work sheds new light on the design of more advanced SA electrodes for efficient energy conversion. Furthermore, the electrosynthesis of C_2H_4 and EtOH enabled by the presented catalysis could provide a highly selective and energetically efficient route to value-added chemicals and fuels using abundant industrial CO as starting material.

Methods

Synthesis of $\text{Ti}_3\text{C}_2\text{T}_x$. Typically, 1 g of Ti_3AlC_2 powder was mixed with 1 g of LiF and 10 mL of HCl, and the obtained mixture was kept stirring for 24 h at 35 °C. The resulting solid residue was washed several times with deionized water and centrifuged at a speed of 1150 × g. Finally, $\text{Ti}_3\text{C}_2\text{T}_x$ was obtained by freeze-drying.

Synthesis of NaBH_4 reduced $\text{Ti}_3\text{C}_2\text{T}_x$ (R- $\text{Ti}_3\text{C}_2\text{T}_x$). For the synthesis of R- $\text{Ti}_3\text{C}_2\text{T}_x$, 50 mL of $\text{Ti}_3\text{C}_2\text{T}_x$ suspension (1 mg mL⁻¹) was mixed with 1 mL of NaBH_4 aqueous solution (10 mg mL⁻¹) and stirred for 30 min. Subsequently, the mixture was ultrasonicated for 1 h, and the R- $\text{Ti}_3\text{C}_2\text{T}_x$ was obtained by centrifugation and freeze-drying.

Synthesis of Cu-SA/ $\text{Ti}_3\text{C}_2\text{T}_x$ and Cu-NC/ $\text{Ti}_3\text{C}_2\text{T}_x$. In a typical synthesis procedure of Cu-SA/ $\text{Ti}_3\text{C}_2\text{T}_x$, 50 mg of $\text{Ti}_3\text{C}_2\text{T}_x$ was firstly dissolved in 50 mL of water in a round-bottom flask, after that, the mixture was sonicated for 30 min to obtain a uniform dispersion. Then, a certain amount of 1 mg mL⁻¹ $\text{CuCl}_2 \cdot 2\text{H}_2\text{O}$ (0.67 mL for Cu-SA/ $\text{Ti}_3\text{C}_2\text{T}_x$ and 2.01 mL for Cu-NC/ $\text{Ti}_3\text{C}_2\text{T}_x$) was added into 25 mL of $\text{Ti}_3\text{C}_2\text{T}_x$ suspension slowly, and electromagnetic stirred for 30 min. Subsequently, the mixture was ultrasonicated for 1 h. After centrifuged and washed with deionized water, the solid residue was vacuum freeze-dried to obtain Cu-SA/ $\text{Ti}_3\text{C}_2\text{T}_x$.

Synthesis of Cu-NP/ $\text{Ti}_3\text{C}_2\text{T}_x$. For the synthesis of Cu-NP/ $\text{Ti}_3\text{C}_2\text{T}_x$ samples, 50 mg of $\text{Ti}_3\text{C}_2\text{T}_x$ was first dissolving in 50 mL of deionized water, and then a certain amount of 1 mg mL⁻¹ $\text{CuCl}_2 \cdot 2\text{H}_2\text{O}$ aqueous solution (6.7, 13.4 or 26.8 mL) was added into the above $\text{Ti}_3\text{C}_2\text{T}_x$ suspension slowly, followed by stirring for 30 min. Then, 1 mL of hydrazine hydrate ($\text{N}_2\text{H}_4 \cdot \text{H}_2\text{O}$) was added into the above resultant mixture quickly, with vigorous stirring for 2 h at room temperature. Subsequently, the resulting solution was centrifuged, and the obtained residue was washed by deionized water. Finally, Cu-NP/ $\text{Ti}_3\text{C}_2\text{T}_x$ was obtained by freeze-drying. The Cu content in the three samples was determined by ICP-OES measurements as 5.2, 9.8, and 20.3 wt%, respectively.

Materials characterizations. TEM and EDX mappings were performed using FEI Talos F200X instruments. Atomic-resolution HAADF-STEM images and EELS were taken using a Titan Themis 60-300 STEM equipment equipped with a spherical probe aberration corrector. XRD was performed on an X-ray diffractometer (Rigaku SmartLab 9 kW) with Cu K α radiation ($\lambda = 0.154598$ nm) at a scan rate of 10° min⁻¹ from 3° to 70°. XPS characterizations were conducted by Thermo Scientific Al K α XPS system (ESCALAB250Xi), and the binding energies were calibrated by setting the measured binding energy of C 1s to 284.8 eV. ICP-OES analysis was conducted on a Thermo iCAP RQ instrument. The elemental analysis was performed by an elemental analyzer (Vario EL cube). CO-DRIFTS measurements were carried out on a Thermo Scientific Nicolet 6700 Fourier transform infrared (FT-IR) spectrometer.

XAFS measurements and analysis details. The Cu K-edge X-ray absorption spectra were collected on the unfocused 20-pole 2 T wiggler side-station beamline 7-3 at the Stanford Synchrotron Radiation Lightsource under standard ring conditions of 3 GeV and ~500 mA. The Si (220) double crystal monochromators were used for energy selection. The components from higher harmonics were diminished after detuning the monochromator by 30–40%. By using cellulose as a binder and diluent, the solid samples were pressed into palettes and installed on a cryogenic sample rod. During data collection, they were kept inside a liquid helium CryoIndustries cryocooler at ~10 K. A detector of Lytle or Canberra Germanium 30-element array was used, and all the EXAFS data were measured to $k = 15 \text{ \AA}^{-1}$ in fluorescence mode. Internal energy was calibrated by simultaneous measurement of the absorption edge of a Cu-foil standard sample which is placed between two ionization chambers situated after the sample probe. The SamView of the Sixpack software was used to process the XAS data obtained from the Germanium detector. The normalization of data was accomplished by subtracting the cubic spline using the Athena program, in which the edge jump was assigned to 1.0. The FT-EXAFS data fitting was completed by the Artemis software. The structural parameters of bond distance (R), coordination numbers (N), and the bond variance (σ^2 , related to the Debye-Waller factor and the static disorders of the scattering atoms) were varied during the fitting process.

Electrochemical COR. Electrocatalytic properties of the catalysts were conducted using an electrochemistry workstation (CHI660D Shanghai Chenhua Instrument Co.) with an H-type electrochemical cell. The catholyte and anolyte compartments were separated using a Nafion-117 membrane to avoid possible diffusion. A graphite rod and a Hg/HgO electrode were used as the counter and reference electrodes, respectively. The electrolyte used for all COR experiments was 1 M KOH. A carbon paper loaded with samples was used as the working electrode. Typically, 6 mg of catalyst and 0.5 mL of Nafion solution (0.05 wt%) were dispersed into 0.5 mL of EtOH (or isopropanol) by sonication for 30 min. After that, the ink was dropped onto the carbon paper and dried naturally.

For the detection of the COR products, the electrolysis was carried out in fresh CO-saturated 1 M KOH aqueous solution for 2 h at each applied potential. During

the electrolysis, CO was continuously delivered into the cathodic compartment at a constant rate of 20 sccm. Polarization curves were recorded by a scan rate of 10 mV s⁻¹. The long-term durability was examined by using a chronoamperometry method.

The cell outlet gas products were analyzed by a gas chromatograph (GC, 7890 Agilent) equipped with a PoraPLOT Q column and a molecular sieve column. A flame ionization detector (FID) and a thermal conductivity detector (TCD) were used to analyze the products.

The Faradaic efficiency of gas species (FE_{gas}) was calculated as follows:

$$\text{FE}_{\text{gas}}(\%) = \frac{N_k \times C_k \times V_{\text{CO}} \times t \times F \times 10^{-3}}{22.4Q} \quad (3)$$

where N_k is the exchanged electron numbers to produce species k , C_k is the concentration of the product, measured by GC; V_{CO} is the CO flow rate; t is electrolysis time; F is the Faradaic constant (96485 C mol⁻¹); Q is the total charge amount.

The liquid products were analyzed using a ¹H NMR spectrum tested on a NMR (Bruker AVANCE AV III 400) equipment with a sensitivity of 480: 1. Standard curves were first made using standard chemicals over the concentration range of interest (EtOH and acetate), with the internal standard DMSO in 1 M KOH⁶⁰. The ¹H NMR spectrum was measured with water suppression via a presaturation method. The linearity of the two standard curves is as high as 0.999 (Supplementary Fig. 15), indicative of good accuracy in determining the concentration of products. In this work, the detection limits of EtOH and acetate were 0.1 and 0.15 μg mL⁻¹, respectively. To quantify the liquid products, 0.5 mL fresh electrolyte electrolyzed at a determined potential for 2 h was mixed with 0.1 mL D₂O and 0.05 μL DMSO. The ratio of the peak areas of the obtained EtOH and acetate to the DMSO peak area were compared to standard curves to quantify the concentrations of the reaction products. Then, the values of the EtOH or acetate yield rate can be derived from the slopes of the curves made by plotting the EtOH or acetate concentrations vs reaction times.

The Faradaic efficiency of liquid products ($\text{FE}_{\text{liquid}}$) was calculated as follows:

$$\text{FE}_{\text{Liquid}}(\%) = \frac{n \times V \times F \times N_k}{Q} \quad (4)$$

where n (mol) is the content of EtOH or acetate, based on the calibration of the NMR; V is the electrolyte volume in the cathodic chamber; F is the Faradaic constant (=96485 C mol⁻¹); N_k is the number of transferred to produce species k ; Q is the total charge amount at different applied potentials.

For the isotope-labeling experiment, the same COR electrolysis was performed except ¹³CO (¹³C 99.99%, Sigma-Aldrich) was used as the feeding gas. The products containing C-isotope was determined by a gas chromatograph (GC) equipped with an Agilent 5977A mass selective (MS) detector. High-purity He (99.99%) was used as the carrier gas.

Computational details. All the DFT calculations were performed using the VASP package with VASPKIT code for post-processing the calculated data. Generalized gradient approximation (GGA) with the Perdew-Burke-Ernzerhof (PBE) functional is employed to treat the exchange-correlation energy. The interaction between core and valence electrons was described by the projected augmented wave (PAW) basis set. A converged cutoff was set to 500 eV. Only the electrons in brackets of Ti [3d²4s²], Cu [3d¹⁰4s¹], C [2s²2p²], O [2s²2p⁴], and H [1s¹] were treated as valence electrons. Implicit solvation corrections were applied, and the electrolyte was incorporated using the Poisson–Boltzmann model implemented in VASPsol⁵², in which the relative permittivity of the media ϵ_r was chosen as 78.4. Zero damping DFT-D3 method was used to investigate weak intermolecular interactions. In geometry optimizations, the force convergence standard was set below 0.02 eV Å⁻¹. The 3 × 3 × 1 Monkhorst–Pack k -point mesh was used for each Cu-SA/ $\text{Ti}_3\text{C}_2\text{T}_x$ and Cu (111) slab optimization. To obtain electronic energy in the ground state accurately, 5 × 5 × 1 grid was used to produce a self-consistent field. The bottom two layers were fixed to implement the free energy calculation of each intermediate. A 15 Å vacuum layer was constructed along the z -axis for each model. Contributions of zero-point energies (ZPE), enthalpy, entropy, and pH to the free energies were considered and calculated. The calculation details of the Gibbs free energy change (ΔG) were expressed as follows:

$$\Delta G = \Delta E + \Delta E_{\text{ZPE}} + \int C_p dT - T\Delta S + \Delta G_{\text{pH}} \quad (5)$$

where ΔE is the electronic energy difference between the free-standing and the adsorption states of the intermediates; $\int C_p dT$ is the enthalpic temperature correction (see details in Supplementary Tables 3 and 4). ΔE_{ZPE} and ΔS are the corrections of zero-point energy and variation of entropy, respectively (see details in Supplementary Tables 3 and 4). Frequencies <50 cm⁻¹ were set to 50 cm⁻¹. ΔG_{pH} is the free energy correction of pH and is calculated according to the equation below:

$$\Delta G_{\text{pH}} = k_B T \times \text{pH} \times \ln 10 \quad (6)$$

where k_B is the Boltzmann constant. pH is set to 14 in this work.

The binding energy of Cu SA ($E_{\text{Cu-SA/Ti}_3\text{C}_2\text{T}_x}^{\text{bind}}$) and the cohesive energy of Cu bulk ($E_{\text{Cu bulk}}^{\text{coh}}$) were calculated by the following equations:

$$E_{\text{Cu-SA/Ti}_3\text{C}_2\text{T}_x}^{\text{bind}} = -\left(E_{\text{Cu-SA/Ti}_3\text{C}_2\text{T}_x} - E_{\text{Ti}_3\text{C}_2\text{T}_x} - E_{\text{Cu-SA}}\right) \quad (7)$$

$$E_{\text{Cu bulk}}^{\text{coh}} = -\frac{E_{\text{Cu bulk}} - nE_{\text{Cu-SA}}}{n} \quad (8)$$

where $E_{\text{Cu-SA}}$, $E_{\text{Cu bulk}}$, $E_{\text{Ti}_3\text{C}_2\text{T}_x}$ and $E_{\text{Cu-SA/Ti}_3\text{C}_2\text{T}_x}$ are the energies of a free single Cu atom, the Cu foil, the $\text{Ti}_3\text{C}_2\text{T}_x$ substrate slab, and Cu-SA/ $\text{Ti}_3\text{C}_2\text{T}_x$ model, respectively; n is the sum of Cu atoms in a Cu conventional cell.

To measure the difficulty of Cu atom migration, the energy barrier (E_b) was calculated according to the following equation:

$$E_b = E_{\text{TS}} - E_{\text{IS}} \quad (9)$$

where E_{TS} is the total energy of transition state configuration; E_{IS} is the total energy of the initial configuration.

The Bader charge analysis was performed to quantitatively estimate the charge state of the Cu atoms in Cu-SA/ $\text{Ti}_3\text{C}_2\text{T}_x$ and Cu_2O .

Transition states of interest were searched by CI-NEB method with an electron step convergence criterion of 10^{-8} eV.

Data availability

The data that support the findings of this study are available within the article (and its Supplementary Information files) and from the corresponding authors upon reasonable request.

Received: 16 February 2020; Accepted: 26 November 2020;

Published online: 11 January 2021

References

- Jouny, M., Hutchings, G. S. & Jiao, F. Carbon monoxide electroreduction as an emerging platform for carbon utilization. *Nat. Catal.* **2**, 1062–1070 (2019).
- Lu, Q. et al. A selective and efficient electrocatalyst for carbon dioxide reduction. *Nat. Commun.* **5**, 3242 (2014).
- Mou, S. et al. Boron phosphide nanoparticles: a nonmetal catalyst for high-selectivity electrochemical reduction of CO_2 to CH_3OH . *Adv. Mater.* **31**, 1903499 (2019).
- Ji, L. et al. Highly selective electrochemical reduction of CO_2 to alcohols on an FeP nanoarray. *Angew. Chem. Int. Ed.* **59**, 758–762 (2020).
- Li, C. W., Ciston, J. & Kanan, M. W. Electroreduction of carbon monoxide to liquid fuel on oxide-derived nanocrystalline copper. *Nature* **508**, 504–507 (2014).
- Cuellar, N. R., Wiesner-Fleischer, K., Fleischer, M., Rucki, A. & Hinrichsen, O. Advantages of CO over CO_2 as reactant for electrochemical reduction to ethylene, ethanol and n-propanol on gas diffusion electrodes at high current densities. *Electrochim. Acta* **307**, 164–175 (2019).
- Zheng, T., Jiang, K. & Wang, H. Recent advances in electrochemical CO_2 -eent conversion on heterogeneous catalysts. *Adv. Mater.* **30**, 1802066 (2018).
- Ripatti, D. S., Veltman, T. R. & Kanan, M. W. Carbon monoxide gas diffusion electrolysis that produces concentrated C_2 products with high single-pass conversion. *Joule* **3**, 240–256 (2019).
- Jouny, M., Luc, W. & Jiao, F. High-rate electroreduction of carbon monoxide to multi-carbon products. *Nat. Catal.* **1**, 748–755 (2018).
- Raciti, D. et al. Low-overpotential electroreduction of carbon monoxide using copper nanowires. *ACS Catal.* **7**, 4467–4472 (2017).
- Zhang, H., Li, J., Cheng, M.-J. & Lu, Q. CO electroreduction: current development and understanding of Cu-based catalysts. *ACS Catal.* **9**, 49–65 (2018).
- Luc, W. et al. Two-dimensional copper nanosheets for electrochemical reduction of carbon monoxide to acetate. *Nat. Catal.* **2**, 423–430 (2019).
- Li, J. et al. Effectively increased efficiency for electroreduction of carbon monoxide using supported polycrystalline copper powder electrocatalysts. *ACS Catal.* **9**, 4709–4718 (2019).
- Jiang, K. et al. Metal ion cycling of Cu foil for selective C–C coupling in electrochemical CO_2 reduction. *Nat. Catal.* **1**, 111–119 (2018).
- Dinh, C.-T. et al. CO_2 electroreduction to ethylene via hydroxide-mediated copper catalysis at an abrupt interface. *Science* **360**, 783–787 (2018).
- Mi, Y. et al. Selective electroreduction of CO_2 to C_2 products over Cu_3N products on nanowires. *ChemElectroChem* **6**, 2393–2397 (2019).
- Ma, S. et al. Electroreduction of carbon dioxide to hydrocarbons using bimetallic Cu–Pd catalysts with different mixing patterns. *J. Am. Chem. Soc.* **139**, 47–50 (2017).
- Cheng, T., Xiao, H. & Goddard, W. A. Nature of the active sites for CO reduction on copper nanoparticles: suggestions for optimizing performance. *J. Am. Chem. Soc.* **139**, 11642–11645 (2017).
- Malkani, A. S., Dunwell, M. & Xu, B. Operando spectroscopic investigations of copper and oxide-derived copper catalysts for electrochemical CO reduction. *ACS Catal.* **9**, 474–478 (2018).
- Zhang, B. W., Wang, Y. X., Chou, S. L., Liu, H. K. & Dou, S. X. Fabrication of superior single-atom catalysts toward diverse electrochemical reactions. *Small Methods* **3**, 1800497 (2019).
- Lü, F. et al. Nitrogen-coordinated single Fe sites for efficient electrocatalytic N_2 fixation in neutral media. *Nano Energy* **61**, 420–427 (2019).
- Lü, F. et al. Electrochemical CO_2 reduction: from nanoclusters to single atom catalysts. *Sustain. Energy Fuels* **4**, 1012–1028 (2020).
- Yang, H. et al. Scalable production of efficient single-atom copper decorated carbon membranes for CO_2 electroreduction to methanol. *J. Am. Chem. Soc.* **141**, 12717–12723 (2019).
- Song, B. et al. Two-dimensional anti-Van't Hoff/Le Bel array AlB_6 with high stability, unique motif, triple Dirac cones, and superconductivity. *J. Am. Chem. Soc.* **141**, 3630–3640 (2019).
- Yang, L.-M. et al. Two-dimensional Cu_2Si monolayer with planar hexacoordinate copper and silicon bonding. *J. Am. Chem. Soc.* **137**, 2757–2762 (2015).
- Liu, J.-H., Yang, L.-M. & Ganz, E. Efficient and selective electroreduction of CO_2 by single-atom catalyst two-dimensional TM–Pc monolayers. *ACS Sustain. Chem. Eng.* **6**, 15494–15502 (2018).
- Liu, J.-H., Yang, L.-M. & Ganz, E. Electrochemical reduction of CO_2 by single atom catalyst TM–TCNQ monolayers. *J. Mater. Chem. A* **7**, 3805–3814 (2019).
- Liu, J.-H., Yang, L.-M. & Ganz, E. Electrochemical reduction of CO_2 by two-dimensional transition metal porphyrin sheets. *J. Mater. Chem. A* **7**, 11944–11952 (2019).
- Liu, J.-H., Yang, L.-M. & Ganz, E. Efficient electrocatalytic reduction of carbon dioxide by metal-doped β 12-borophene monolayers. *RSC Adv.* **9**, 27710–27719 (2019).
- Liu, J.-H., Yang, L.-M. & Ganz, E. Two-dimensional organometallic $\text{TM}_3\text{C}-12\text{S}12$ monolayers for electrocatalytic reduction of CO_2 . *Energy Environ. Mater.* **2**, 193–200 (2019).
- Naguib, M. et al. Two-dimensional nanocrystals produced by exfoliation of Ti_3AlC_2 . *Adv. Mater.* **23**, 4248–4253 (2011).
- Naguib, M., Mochalin, V. N., Barsoum, M. W. & Gogotsi, Y. 25th anniversary article: MXenes: a new family of twoof Ti metal-doped β 12-b. *Adv. Mater.* **26**, 992–1005 (2014).
- Alhabeab, M. et al. Guidelines for synthesis and processing of two-dimensional titanium carbide ($\text{Ti}_3\text{C}_2\text{T}_x$ MXene). *Chem. Mater.* **29**, 7633–7644 (2017).
- Zhao, D. et al. MXene (Ti_3C_2) vacancy-confined single-atom catalyst for efficient functionalization of CO_2 . *J. Am. Chem. Soc.* **141**, 4086–4093 (2019).
- Zhao, S. et al. Isolated single-atom Pt sites for highly selective electrocatalytic hydrogenation of formaldehyde to methanol. *J. Mater. Chem. A* **8**, 8913–8919 (2020).
- Liu, X. et al. Nanoporous Zn-doped Co_3O_4 sheets with single-unit-cell-wide lateral surfaces for efficient oxygen evolution and water splitting. *Nano Energy* **44**, 371–377 (2018).
- Garcia, A. et al. Polymer grafting by inkjet printing: a direct chemical writing toolset. *Adv. Funct. Mater.* **23**, 3668–3674 (2013).
- Kumar, M., Satpati, B. & Som, T. Revealing multimode resistive switching in Cu-0 nanostructures using conductive atomic force microscopy. *Appl. Surf. Sci.* **454**, 82–86 (2018).
- Gu, J., Hsu, C.-S., Bai, L., Chen, H. M. & Hu, X. Atomically dispersed Fe^{3+} sites catalyze efficient CO_2 electroreduction to CO. *Science* **364**, 1091–1094 (2019).
- Liu, P. et al. Photochemical route for synthesizing atomically dispersed palladium catalysts. *Science* **352**, 797–800 (2016).
- Karapinar, D. et al. Electroreduction of CO_2 on single-site copper-nitrogen-doped carbon material: selective formation of ethanol and reversible restructuring of the metal sites. *Angew. Chem. Int. Ed.* **58**, 15098–15103 (2019).
- Wang, L. et al. Electrochemically converting carbon monoxide to liquid fuels by directing selectivity with electrode surface area. *Nat. Catal.* **2**, 702–708 (2019).
- Pang, Y. et al. Efficient electrocatalytic conversion of carbon monoxide to propanol using fragmented copper. *Nat. Catal.* **2**, 251–258 (2019).
- Chen, R. et al. Highly selective production of ethylene by the electroreduction of carbon monoxide. *Angew. Chem. Int. Ed.* **59**, 154–160 (2020).
- Han, Z., Kortlever, R., Chen, H.-Y., Peters, J. C. & Agapie, T. CO_2 reduction selective for $\text{C}\geq 2$ products on polycrystalline copper with N-substituted pyridinium additives. *ACS Cent. Sci.* **3**, 853–859 (2017).
- Crowley, S. & Castaldi, M. J. Mechanistic insights into catalytic ethanol steam reforming using isotope-labeled reactants. *Angew. Chem. Int. Ed.* **55**, 10650–10655 (2016).
- Lum, Y. & Ager, J. W. Evidence for product-specific active sites on oxide-derived Cu catalysts for electrochemical CO_2 reduction. *Nat. Catal.* **2**, 86–93 (2019).

48. Wang, T. et al. Cu,N-codoped carbon nanodisks with biomimic stomata-like interconnected hierarchical porous topology as efficient electrocatalyst for oxygen reduction reaction. *Small* **15**, 1902410 (2019).
49. Zhang, T. et al. Single atomic Cu-N₂ catalytic sites for highly active and selective hydroxylation of benzene to phenol. *iScience* **22**, 97–108 (2019).
50. Bai, X. et al. Insight into the catalytic activity of MXenes for hydrogen evolution reaction. *Sci. Bull.* **63**, 1397–1403 (2018).
51. Gao, G., O'Mullane, A. P. & Du, A. 2D MXenes: a new family of promising catalysts for the hydrogen evolution reaction. *ACS Catal.* **7**, 494–500 (2017).
52. Letchworth-Weaver, K. & Arias, T. Joint density functional theory of the electrode-electrolyte interface: application to fixed electrode potentials, interfacial capacitances, and potentials of zero charge. *Phys. Rev. B* **86**, 075140 (2012).
53. Goodpaster, J. D., Bell, A. T. & Head-Gordon, M. Identification of possible pathways for C–C bond formation during electrochemical reduction of CO₂: new theoretical insights from an improved electrochemical model. *J. Phys. Chem. Lett.* **7**, 1471–1477 (2016).
54. Schouten, K. J. P., Qin, Z., Pérez Gallent, E. & Koper, M. T. Two pathways for the formation of ethylene in CO reduction on single-crystal copper electrodes. *J. Am. Chem. Soc.* **134**, 9864–9867 (2012).
55. Calle Chem, F. & Koper, M. T. Theoretical considerations on the electroreduction of CO to C₂ species on Cu (100) electrodes. *Angew. Chem. Int. Ed.* **52**, 7282–7285 (2013).
56. Garza, A. J., Bell, A. T. & Head-Gordon, M. Mechanism of CO₂ reduction at copper surfaces: pathways to C₂ products. *ACS Catal.* **8**, 1490–1499 (2018).
57. Schouten, K. J. P., Gallent, E. P. & Koper, M. T. The electrochemical characterization of copper single-crystal electrodes in alkaline media. *J. Electroanal. Chem.* **699**, 6–9 (2013).
58. Schouten, K. J. P., Pérez Gallent, E. & Koper, M. T. Structure sensitivity of the electrochemical reduction of carbon monoxide on copper single crystals. *ACS Catal.* **3**, 1292–1295 (2013).
59. Li, Y. C. et al. Binding site diversity promotes CO₂ electroreduction to ethanol. *J. Am. Chem. Soc.* **141**, 8584–8591 (2019).
60. Kuhl, K. P., Cave, E. R., Abram, D. N. & Jaramillo, T. F. New insights into the electrochemical reduction of carbon dioxide on metallic copper surfaces. *Energy Environ. Sci.* **5**, 7050–7059 (2012).
61. Hoang, T. T. et al. Nanoporous copper–silver alloys by additive-controlled electrodeposition for the selective electroreduction of CO₂ to ethylene and ethanol. *J. Am. Chem. Soc.* **140**, 5791–5797 (2018).
62. Zhang, J. et al. Single platinum atoms immobilized on an MXene as an efficient catalyst for the hydrogen evolution reaction. *Nat. Catal.* **1**, 985–992 (2018).
63. Wang, Y. et al. Adsorption-energy-based activity descriptors for electrocatalysts in energy storage applications. *Natl Sci. Rev.* **5**, 327–341 (2018).

Acknowledgements

This work was financially supported by the National Key R&D Program of China (2017YFA0700104), the National Natural Science Foundation of China (22075211, 51971157, 51808037, 21601136, and 51761165012), the Tianjin Science Fund for

Distinguished Young Scholars (19JCJQC61800), and the Science and Technology Development Fund of Tianjin Education Commission for Higher Education (No. 2018KJ126). The authors acknowledge Beijing PARATERA Tech CO., Ltd. for providing HPC resources that have contributed to the research results reported within this paper. The authors also thank Stanford Synchrotron Radiation Lightsource (SSRL) BL7-3 for providing the beam time. R.C. acknowledges support from DOE funded LDRD program and SSRL.

Author contributions

X.J.L. and X.P.S. proposed and designed the electrocatalysts. H.H.B., Y.Q., and X.Y.P. co-synthesized the catalyst samples and carried out the electrochemical measurements, to which Y.Y.M. and J.Q.S. assisted. Y.Q., J.A.W., and S.Z.Z. conducted the DFT-calculations. R.C. performed the XAS experiments. H.H.B., X.Y.P., and Y.F.L. analyzed the XAS results. J.Q.R. and L.C.Z. assisted in analyzing the experimental data. X.J.L., J.L., and X.P.S. co-performed the experimental design and the mechanism analysis, and they co-supervised the whole project. All authors discussed the results.

Competing interests

The authors declare no competing interests.

Additional information

Supplementary information is available for this paper at <https://doi.org/10.1038/s41467-020-20336-4>.

Correspondence and requests for materials should be addressed to X.L., R.C. or X.S.

Peer review information *Nature Communications* thanks Liming Yang and the other, anonymous, reviewer(s) for their contribution to the peer review of this work. Peer reviewer reports are available.

Reprints and permission information is available at <http://www.nature.com/reprints>

Publisher's note Springer Nature remains neutral with regard to jurisdictional claims in published maps and institutional affiliations.



Open Access This article is licensed under a Creative Commons Attribution 4.0 International License, which permits use, sharing, adaptation, distribution and reproduction in any medium or format, as long as you give appropriate credit to the original author(s) and the source, provide a link to the Creative Commons license, and indicate if changes were made. The images or other third party material in this article are included in the article's Creative Commons license, unless indicated otherwise in a credit line to the material. If material is not included in the article's Creative Commons license and your intended use is not permitted by statutory regulation or exceeds the permitted use, you will need to obtain permission directly from the copyright holder. To view a copy of this license, visit <http://creativecommons.org/licenses/by/4.0/>.

© The Author(s) 2021